Complex transport and magnetism of the ternary boride $YbPt_5B_2$

L. Salamakha,[1,2] O. Sologub,[1] A. Riss,[1] H. Michor,[1] H. Müller,[1] B. Stöger,[3]
G. Giester,[4] P. Rogl,[5] A. Sakai,[6] P. Gegenwart,[6] and E. Bauer[1,*]
[1]*Institute of Solid State Physics, TU Wien, A-1040 Vienna, Austria*
[2]*Department of Physics of Metals, L'viv National University, L'viv, Ukraine*
[3]*X-Ray Center, TU Wien, A-10460 Vienna, Austria*
[4]*Institute of Mineralogy and Crystallography, University of Vienna, A-1090 Vienna, Austria*
[5]*Institute of Materials Chemistry Research, University of Vienna, A-1090 Vienna, Austria*
[6]*Center for Electronic Correlations and Magnetism, University of Augsburg, D-86159 Augsburg, Germany*

(Received 13 January 2022; revised 7 April 2022; accepted 7 April 2022; published 11 May 2022)

Novel ternary platinum borides $YbPt_5B_2$ and $LuPt_5B_2$ have been synthesized by arc melting of constituent elements and subsequent annealing at 1020 K. The unit cell of $YbPt_5B_2$ [$YbPt_5B_2$ type, monoclinic space group $C2/m$, $a = 15.4982(6)$ Å, $b = 5.5288(3)$ Å, $c = 5.5600(3)$ Å, $\beta = 105.367(3)^\circ$, single-crystal x-ray diffraction data] is composed of two structural fragments alternating along the a axis and extending infinitively along the b axis: (i) columns of face-fused, boron-filled, and empty edge-connected trigonal metal prisms, and (ii) zigzag chains of B-filled trigonal prisms connected by common edges. $LuPt_5B_2$ was found to be isotypic (Rietveld refinement of powder x-ray diffraction data). $YbPt_5B_2$ exhibits two magnetic phase transitions at $T_{\mathrm{mag1}} \sim 8$ K and $T_{\mathrm{mag2}} \sim 4$ K as deduced from specific heat, magnetostriction, electric resistivity, and magnetization data. The Kadowaki-Woods ratio of 1.22×10^{-5} $\mu\Omega$ cm(mol K/mJ)^2 classifies $YbPt_5B_2$ as a heavy fermion system. A magnetic phase diagram was established, using magnetostriction and magnetoresistance data. Nonmagnetic $LuPt_5B_2$ is characterized by a simple metallic behavior.

DOI: 10.1103/PhysRevB.105.205112

I. INTRODUCTION

Numerous borides in very many different material families have been studied since decades, mainly because of an immense variety of ground states and sophisticated physical features that have been obtained, but also because of the vast range of daily-life applications, reaching from steel to pharmaceuticals. Twenty-one years ago, in 2001, MgB_2, a binary boride with a quite simple hexagonal crystal structure, was unexpectedly found as a high-temperature superconductor ($T_c \sim 40$ K) [1].

Metal borides, in many aspects, deviate from standard concepts in physical chemistry. Very frequently, they do not follow concepts of valency, either in stoichiometry or in structure [2]. With respect to stoichiometry, metal borides stretch from low-boron systems like M_5B, to compounds extremely rich in boron, such as MB_{66} or MB_{99}, where M represents a metal. Because of these extended compositional ranges, there is a wide variety of crystallographic structures [3]. The distribution of boron atoms in the crystallographic unit cells ranges from isolated boron atoms to pairs, chains, and three-dimensional connected networks in the boron-rich borides. Covalent bonding of the boron atoms provokes the commonly observed high hardness and high melting points known for borides.

Among the many families of borides, the rare-earth (RE)-based ones are known for their diverse physical features like magnetically ordered phases, exotic types of ordering such as quadrupolar ordering, intermediate valence, Kondo-based or topologically protected materials, heavy fermion behavior, or superconductivity in coexistence with long range magnetic order [4–11]. Several of such features are observed in systems with RE = Ce, Yb, because of the respective unstable $4f^1$ and $4f^{13}$ electronic configurations (EC), which may easily modify towards the nonmagnetic $4f^0$ and $4f^{14}$ states.

Binary and ternary RE borides constitute sizable families of compounds with large member numbers. The most common structure type within ternary transition-metal (T)-rich RE borides is $CeCo_3B_2$, with a $CaCu_5$-type superstructure [$P6/mmm$, Ce in $1a$ (0, 0, 0); Co in $3g$ (1/2, 0, 1/2), and B in $2c$ (1/3, 2/3, 0)] [12–14]. In this structure, boron atoms are located in the center of trigonal Co prisms with three Ce atoms centering the lateral prism faces, [BCo_6Ce_3]. In terms of trigonal prisms arrangement, the structure can be viewed as a 3D framework formed by edge-shared infinite columns of base-linked boron-filled Co trigonal prisms.

Extensive studies of RE-T-B systems with transition metals such as Co, Ni, Ru, Rh, Os, Ir hitherto revealed a large number of complex $CaCu_5$-derivative structures, where the $CeCo_3B_2$-type slabs intergrow with slabs of the binary $CaCu_5$, Laves phases, or $ThCr_2Si_2$-type structures [12–18]. On the other hand, several structure variants of the $CeCo_3B_2$ type have been reported for ternary alkaline earth (AE) and alkali (A) borides with platinum ($AE_{0.67}Pt_3B_2$, AE = Ca, Sr, Ba [19], $LiPt_3B$, $NaPt_3B_{1+x}$, and $Na_3Pt_9B_5$ [20]) exhibiting notable structural diversity and exceptional physical properties (e.g., superconductivity at 5.6 K for the Ba-containing

---

[*] bauer@ifp.tuwien.ac.at

member of $AE_{0.67}Pt_3B_2$ superconducting series [19]), while the RE-Pt-B systems showed an astonishing lack of information. Only few ternary rare-earth platinum borides structurally related to $CaCu_5$-type structure have been found and characterized: $REPt_4B$ ($CeCo_4B$ type, RE = La−Nd, Eu) [15], $Eu_3Pt_7B_2$ ($Ca_3Al_7Cu_2$ type), and $Eu_5Pt_{18}B_{6-x}$ (own structure type) [21]; among them the $EuPt_4B$ and $Eu_3Pt_7B_2$ were found to order magnetically at 36 and 57 K, respectively. For $EuPt_4B$ a mixed-valence state of the Eu atom was found via magnetic and specific-heat measurements, while the Sommerfeld value of the specific heat of Eu_3Pt_7B was found to be extraordinarily large, on the order of 0.2 J/mol K^2 [21].

The aim of the present study is to report the structure and physical properties of a $CeCo_3B_2$-type derivative ytterbium platinum boride, $YbPt_5B_2$, as well as of an isotypic compound with Lu. Ytterbium is well known for its divalent, trivalent, or intermediate valence state in different compounds. When Yb is divalent ($4f^{14}$), as is the case in metallic Yb, it is nonmagnetic (total angular momentum $j = 0$) and has a larger atomic radius compared to that of the generally trivalent rare-earth elements. Divalent Yb behaves almost like an alkaline-earth element (e.g., Mg, Ca). In contrast, trivalent Yb has an atomic radius, which follows the lanthanide contraction. It is magnetic, $j = 7/2$, and carries an effective moment, $\mu_{\mathrm{eff}} = 4.54\ \mu_{\mathrm{B}}$. If ytterbium exhibits a valence state intermediate between divalent and trivalent, both the radius and the effective moment of the Yb ion may adopt intermediate values. The resulting numerous physical phenomena attributed to instabilities of the electronic configuration $4f^n$ ($n = 13, 14$) are highly sensitive to the chemical environment (changes in the crystallographic and electronic environment of the Yb ion due to other constituents in a periodic lattice) and external impacts (temperature, pressure, or magnetic field) as numerously reported for different classes of ytterbium compounds, both from experiments and theoretical works [22–32].

Up to now, the information on compound formation and their physical properties in Yb-Pt-B systems is sparse: the only available data exist on $REPt_2B$ ($CePt_2B$-type structure). The Yb-containing member of this series exhibits a weak Kondo effect in the presence of long-range magnetic order, which evolves in a crystalline electric field (CEF) doublet as ground state. The complex ferromagnetic phase below 5.6 K and a spin reorientation at about 1.5 K were determined to be a consequence of the Dzyaloshinskii-Moriya interaction, established because of the absence of inversion symmetry in the crystal structure of $YbPt_2B$ [33]. Because of the absence of any correlation between the remaining Yb-T-B systems and Yb-Pt-B, the discovery of the compound $YbPt_5B_2$, structurally related to the $CeCo_3B_2$ structure, is intriguing in view of the specific behavior of Yb. Some preliminary results were briefly presented at a conference [34].

II. EXPERIMENT DETAILS

A. Sample preparation, structural and electronic characterization

1. Synthesis

Samples were prepared by argon arc melting proper amounts of constituent elements using Ti as getter material. Yb-weight losses were compensated by adding extra amounts of Yb before melting. For homogeneity, the samples were remelted several times. Subsequently, the samples were wrapped in Mo foil, sealed in evacuated silica tubes, and heat treated for 10 d at 1020 K. Powder x-ray diffraction data regarding $YbPt_5B_2$ are summarised in Fig. 1.

2. X-ray diffraction studies

The crystal structure of $YbPt_5B_2$ was studied using single-crystal x-ray diffraction data (a four-circle Nonius Kappa charge-coupled-device diffractometer, MoK_α radiation) [35]. Data collection and refinement parameters are presented in Table I and in the Supplemental Material Table 1S [36]; interatomic distances are listed in the Supplemental Material, Table 2S [36]. X-ray powder diffraction patterns collected from $YbPt_5B_2$ and $LuPt_5B_2$ alloys employing a Guinier-Huber image plate system with monochromatic Cu $K\alpha_1$ radiation ($8^\circ < 2\theta < 100^\circ$) were analyzed using FULLPROF

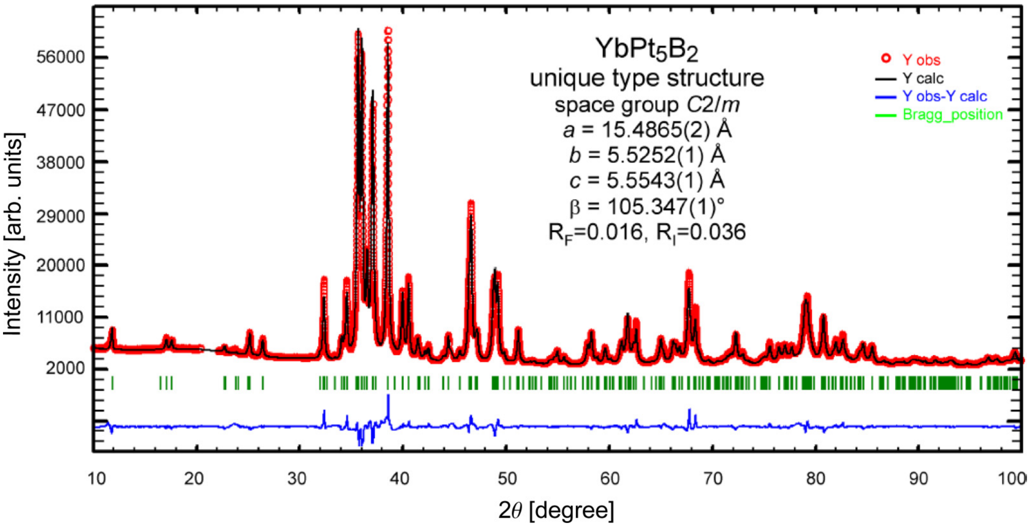

FIG. 1. X-ray powder diffraction pattern of $YbPt_5B_2$. The solid line derives from the Rietveld refinement. Y_{obs}-Y_{calc} is the intensity difference between experimental data and Rietveld calculations.

TABLE I. Single-crystal structure data for $YbPt_5B_2$ [own structure type, space group $C2/m$ (no. 12), $Z = 4$, $a = 15.4982(6)$ Å, $b = 5.5288(3)$ Å, $c = 5.5600(3)$ Å, $\beta = 105.367(3)°$].

Nominal composition	$Yb_{12.5}Pt_{62.5}B_{25}$
Formula from refinement	$YbPt_5B_2$
Theta range	$3.93° < \theta < 33.49°$
Crystal size	$35 \times 35 \times 20\ \mu m^3$
Reflections in refinement	$798\ F_o > 2\sigma(F_o)$ of 970
Mosaicity	<0.4
Number of variables	38
Reliability factors	$R_F = \Sigma\lvert F_0 - F_c\rvert/\Sigma F_0 = 0.034$, GOF $= 1.003$
Extinction (Zachariasen)	0.00060(4)
Yb1[a] in $4i(x, 0, z)$; U_{eq}[b,c]	$x = 0.32799(4)$, $z = 0.6694(1)$; 0.0062(2)
Pt1 in $8j(x, y, z)$; U_{eq}	$x = 0.33345(2)$, $y = 0.25253(8)$, $z = 0.16729(7)$; 0.0048(1)
Pt2 in $4i(x, 0, z)$; U_{eq}	$x = 0.13766(4)$, $z = 0.3645(1)$; 0.0050(2)
Pt3 in $4h(0, y, 1/2)$; U_{eq}	$y = 0.2462(1)$; 0.0030(1)
Pt4 in $4g(0, y, 0)$; U_{eq}	$y = 0.2448(1)$; 0.0044(2)
B1 in $4i(x, 0, z)$; U_{iso}	$x = 0.224(1)$, $z = 0.150(3)$; 0.004(2)
B2 in $4i(x, 0, z)$; U_{iso}	$x = 0.446(1)$, $z = 0.206(3)$; 0.004(2)
Residual density, max; min [el./nm^3] $\times 10^3$	5.46; −5.24
Structure solution/refinement	WINGX program system[d]

[a] Occupation factors for all atom sites are equal to 1.
[b] U_{eq} is defined as one-third of the trace of the orthogonalized U_{ij} tensor.
[c] Anisotropic atom displacement parameters U_{ij} are listed in the Supplemental Material, Table S1 [36].
[d] Reference [37].

[38,39]. Rietveld refinements with the structural model obtained from the single crystal yielded excellent agreement for both samples (see Fig. 1 and Supplemental Material, Fig. 1S, Table 3S [36]).

3. Electronic structure

Density-functional theory (DFT) calculations have been carried out, employing the Vienna *Ab initio* Simulation Package (VASP) [40,41] with the projector augmented-wave potential construction [42,43]. The exchange-correlation potential was calculated within the generalized-gradient approximation using the Perdew-Burke-Ernzerhof form [44]. The structure was relaxed using 11^3 k points with a convergence threshold of 10^{-6} eV. A denser grid of 16^3 k points was used for the calculation of the electronic density of states (DOS), while the band structure was evaluated on 70 k points along each direction.

B. Magnetic, transport, and thermal measurements

Temperature-dependent magnetization measurements between 2 K and room temperature were carried out in a superconducting quantum interference device magnetometer (Cryogenic S600) and isothermal magnetization measurements in fields up to 6 T. Electrical resistivity and magnetoresistivity of bar-shaped samples (about $1 \times 1 \times 5$ mm^3) were measured using a four-probe AC-bridge method in the temperature range from 0.4 K to room temperature and fields up to 12 T. Contacts were made of spot-welded gold wires with a diameter of 50 μm. Low-temperature specific-heat data were measured using a standard heat pulse technique in a semiadiabatic ^{3}He calorimeter in the range between 0.3 and 9 K, at zero and applied magnetic fields up to 9 T and extended to 0.15 K in a dilution refrigerator by utilizing the quasiadiabatic thermal relaxation method. A homemade adiabatic calorimeter was employed for the measurements between 2.5 and 100 K in fields up to 9 T. Thermal expansion and longitudinal magnetostriction had been measured in the temperature range from 3.25 to 300 K in magnetic fields up to 9 T employing a capacitive method with tilted plates [45]. For analysis of physical properties of $YbPt_5B_2$, specific heat, magnetic susceptibility, and electrical resistivity had been studied for its nonmagnetic homologue $LuPt_5B_2$. Prior to the bulk property measurements, Rietveld refinements and electron microprobe analyses have been performed, confirming the phase composition, the equal distribution of grains, and sample purity of the polycrystalline material used.

III. RESULTS AND DISCUSSION

A. Crystal structure

The crystal structure of $YbPt_5B_2$ (Fig. 2) represents a prototype of ternary rare-earth borides. In terms of atoms arrangement, the metal atoms built trigonal prisms which interlink to form two structural blocks alternating infinitively along the a axis (Fig. 2). In block **A**, the layer of boron-centered trigonal prisms of platinum atoms [$B2Pt_6$] connected via common edges (Pt3-Pt3 and Pt4-Pt4) join in the [010] direction by common triangular faces with empty [Pt_6] trigonal prisms. In block **B**, the distorted boron-filled trigonal prisms [$B1Pt_5Yb_1$] are coupled via common Pt1-Pt1 edges to form zigzag chains running along the b axis. With respect to the prism in block **A**, where the prisms axes coincide with the b axis, the prisms in block **B** are rotated by 90°. The interlinkage of both blocks along the x direction is realized via common Pt1-Pt1 edges of triangular prisms. The arrangement of trigonal prisms in block **A** of the $YbPt_5B_2$ structure corresponds to that in the structure of $NaPt_3B$ [20]

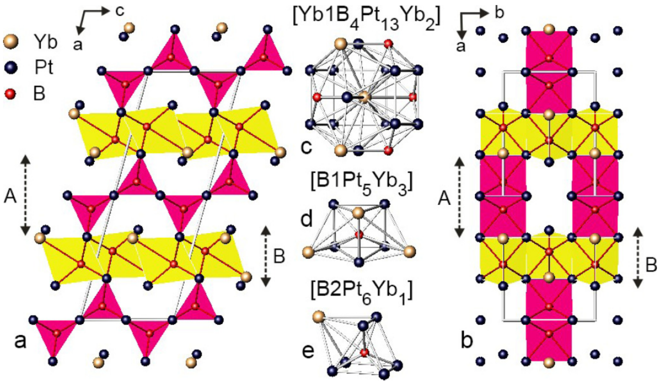

FIG. 2. (a), (b) Crystal structure of $YbPt_5B_2$ viewed in two different orientations to highlight arrangement of trigonal prisms. B1 and B2 filled trigonal prisms are indicated by yellow and red, respectively. Empty [Pt_6] prisms in (b) are left open. (c)–(e) Coordination polyhedra of atoms Yb1, B1, and B2.

(B-deficient variant of $CeCo_3B_2$) where every second layer of edge-connected [Pt_6] trigonal prisms in the unit cell is boron centered; separated columns of zigzag-oriented trigonal prism filled by boron are found in the structure of $SrPd_4B$ [46] (Supplemental Material, Fig. 2S [36]).

Due to the presence of Yb-B contacts, the B1 and B2 trigonal prisms are capped with two and one Yb atoms, respectively (Fig. 2). The coordination number of Yb is 19; the contact distance between Yb atoms ($d_{\mathrm{Yb-Yb}} = 3.8237$ Å) is slightly smaller than that in pure divalent ytterbium (3.88 Å [47]). Empty [Pt_6] prisms in block **A** are compressed along the b axis as compared to boron-filled prisms and exhibit the shortest Pt-Pt distances in the structure (within 2.7070–2.7365 Å for Pt4-Pt4, Pt3-Pt3, and Pt1-Pt1). The shortest Pt-B interatomic distance ($d_{\mathrm{B1-Pt2}} = 2.015$ Å, block **B**) in $YbPt_5B_2$ compares well with the Pt-B distances observed for binary platinum borides ($d_{\mathrm{B-Pt}} = 2.175$ Å in Pt_3B_2 [48] and $d_{\mathrm{B-Pt}} = 2.121$ Å in Pt_2B [49]). There are no boron-boron contacts.

B. Electronic structure of $LuPt_5B_2$

In order to classify the ternary compounds, the electronic density of states and the electron dispersion were calculated using DFT in terms of the software package VASP [40,41]. To avoid Coulomb correlation problems, the calculations are restricted to $LuPt_5B_2$, which appears to be a simple compound, with only weak correlations among electrons. Shown in Figs. 3(a) and 3(b) are the DOS and the electron band structure along high-symmetry lines of the Brillouin zone of $LuPt_5B_2$, respectively. The electronic density of states in the vicinity of the Fermi energy is characterized by relatively smooth structures, a low value of the density of states at Fermi energy, $N(E_F) \sim 2.2$ states/eV, and a positive slope of the $N(E)$ at $E = E_F$. The small, but finite DOS in the proximity of E_F is predominantly a result of Pt d-state contributions. The electronic band structure near the Fermi energy is displayed in Fig. 3(b). There are several conduction and valence bands, crossing the Fermi energy. In addition, these bands are quite dispersive, referring to large charge-carrier velocities and thus to a large mobility of the charge carriers. In fact, the electrical resistivity of $LuPt_5B_2$ behaves as typical simple metal with quite low absolute values.

C. Thermodynamic and transport properties of $REPt_5B_2$

1. Susceptibility

The magnetic susceptibility of $YbPt_5B_2$ was measured between $T = 2.8$ K and room temperature and in applied fields up to 3 T [Figs. 4(a) and 4(b)]. In the high-temperature (HT) range, the results are properly described employing the modified Curie-Weiss law, $\chi = \chi_0 + C/(T - \theta_p)$; a least-squares fit [solid line, Fig. 4(a)] reveals $\mu_{\mathrm{eff}} = 4.14\ \mu_B$, close to the value of a free Yb^{3+} ion as well as $\chi_0 = 0.001$ emu/mol and a negative paramagnetic Curie temperature of $\theta_p = -21$ K. The latter refers to antiferromagnetic interactions among the Yb $4f$ moments and/or Kondo interactions. At low temperatures and low fields, the magnetic susceptibility of $YbPt_5B_2$ is characterized by two anomalies, a sharp kink around

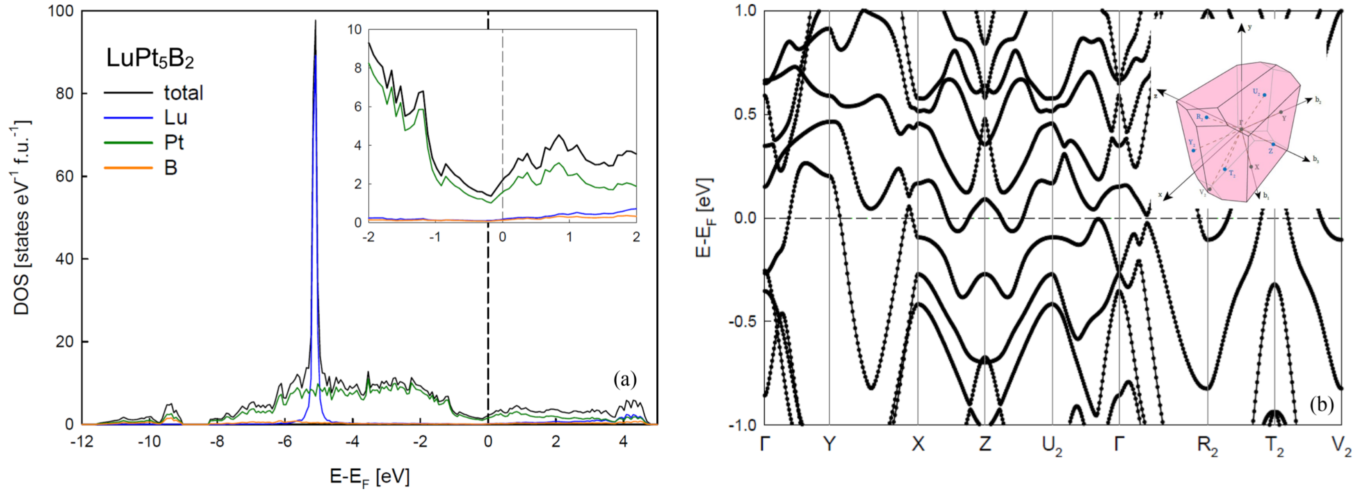

FIG. 3. (a) Energy-dependent electronic density of states of $LuPt_5B_2$ above and below the Fermi energy (marked as dashed vertical line). The inset reveals a decomposition of $N(E)$ with respect to its elemental contributions. (b) Electron dispersion of $LuPt_5B_2$ along high-symmetry directions of the monoclinic crystal structure. The inset sketches the first Brillouin zone of $LuPt_5B_2$ with principal directions and high-symmetry points [50]. A magnified representation is shown in the Supplemental Material, Fig. S3 [36].

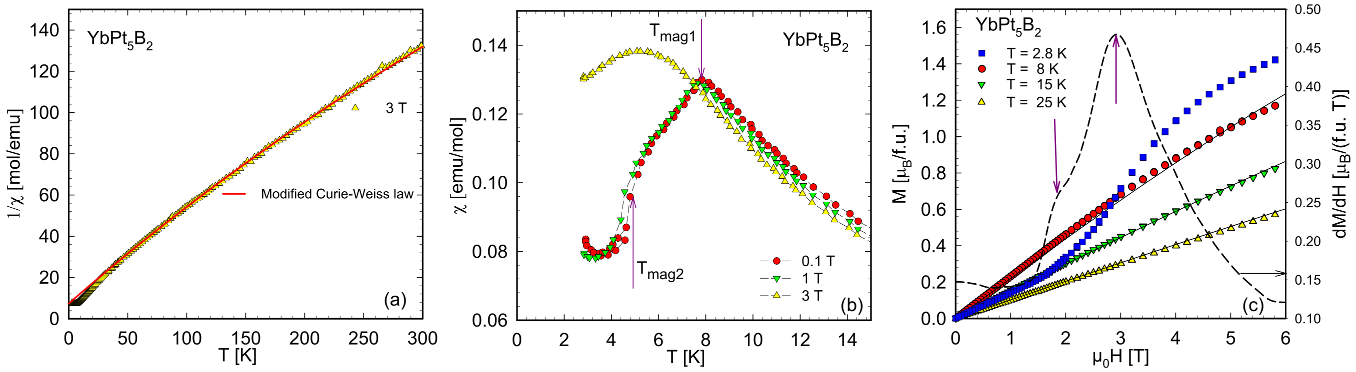

FIG. 4. (a) Temperature-dependent inverse magnetic susceptibility, $1/\chi$, of YbPt$_5$B$_2$. The solid line represents a least-squares fit employing a modified Curie-Weiss model. (b) Low-temperature magnetic susceptibility, χ, of YbPt$_5$B$_2$ measured at different magnetic fields. (c) Field-dependent magnetization curves of YbPt$_5$B$_2$ taken at different temperatures. The dashed line (referring to the right axis) corresponds to $dM/d(\mu_0 H)$ at $T = 2.8$ K, with arrows highlighting the field-induced phase transitions. The solid lines represent results regarding the isothermal magnetization in terms of a mean-field model (see text).

$T_{\rm mag1} = 7.8$ K, which is attributed to a second-order magnetic phase transition and a sharp drop at $T_{\rm mag2} = 4.4$ K in Fig. 4(b). An applied magnetic field shifts both transitions to lower temperatures, revealing antiferromagnetism in both cases. At 3 T, the low-temperature phase transition is no longer observed in $\chi(T)$, at least for temperatures above 2.8 K. Noticeably, the upturn in $\chi(T)$ at very low temperatures (LT) is suppressed with increasing fields, referring to a very small amount of magnetic impurities as origin.

2. *Magnetization*

The results of isothermal magnetization measurements, M, of YbPt$_5$B$_2$ are summed up in Fig. 4(c), showing no signs of saturation for magnetic fields up to 6 T at temperatures as low as 2.8 K ($M = gj\mu_{\rm B} = 4\,\mu_{\rm B}$, where $g = 8/7$ and $j = 7/2$ are the Landé factor and the total angular momentum of the free ion Yb^{3+}, respectively). The absence of saturation relates to the presence of CEF effects, splitting the eightfold degenerate ground state into four doublets; the excited ones become thermally populated only at higher temperatures. The isothermal magnetization curve at $T = 2.8$ K, i.e., below both phase transitions, is characterized by an initial slope, which is smaller than the one slightly above $T_{\rm mag1}$, and by distinct features around 2 and 3 T. A first derivative of the magnetization data with respect to the externally applied magnetic field, $dM/d(\mu_0 H)$, emphasizes these anomalies [dashed line, Fig. 4(c)], which can be referred to field-induced metamagnetic transitions which may relate to two subsequent metamagnetic transitions of the initial magnetic structure or to one metamagnetic transition with significant- anisotropy of the critical magnetic field. The fact that for $\mu_0 H \to 0$ the magnetization M vanishes, signifies an antiferromagnetic ground state.

Externally applied fields rearrange the magnetic structure in such a manner that the resulting magnetic moments become more favorably aligned with respect to the field direction and, simultaneously, alter the CEF ground-state wave function towards an increasing magnetic moment. The combination of both effects seems responsible for the steady increase (beyond 6 T) of the 2.8 K isothermal magnetization in Fig. 4(c). The solid lines in Fig. 4(c) represent model curves of the isothermal magnetization in the paramagnetic temperature range based on the molecular-field theory in terms of an antiferromagnetic scenario. The parameters obtained are an effective magnetic moment $j_{\rm eff} = 1/2$ and a corresponding Landé factor $g_{\rm eff} = 4.25$. The $1/2$ scenario once again indicates a CEF doublet as ground state.

3. *Specific heat*

Results of the temperature-dependent specific heat, $C_{\rm p}$, of nonmagnetic LuPt$_5$B$_2$ are shown in Fig. 5(a) as $C_{\rm p}/T$ vs T; the absence of anomalies in the temperature range studied manifests, at least down to 2.5 K, a nonsuperconducting metal. The LT specific-heat data ($T < 6$ K) could be well described by $C_{\rm p} = \gamma T + \beta T^3$, yielding a Sommerfeld coefficient $\gamma = 6.6$ mJ/mol K^2 and a LT Debye temperature $\theta_{\rm D}^{\rm LT} \sim 279$ K. For the entire temperature range, a combination of Debye and Einstein terms is used to account for the phonon contribution of LuPt$_5$B$_2$, i.e.,

$$C_{\rm ph}(T) = \frac{9R}{\omega_D^3}\int_0^{\omega_{\rm D}} \frac{\omega^2\left(\frac{\omega}{2T}\right)^2}{\sinh^2\left(\frac{\omega}{2T}\right)}d\omega + \sum_i c_i R \frac{\left(\frac{\omega_{E_i}}{2T}\right)^2}{\sinh^2\left(\frac{\omega_{E_i}}{2T}\right)}. \quad (1)$$

Here, ω refers to the phonon frequencies; $\hbar\omega_{\rm D} = k_{\rm B}\theta_{\rm D}$ and $\hbar\omega_{Ei} = k_B\theta_{Ei}$ define the Debye and Einstein temperatures of the ith branch, respectively. $\Sigma_i c_i = 21$ is the number of optical branches of the phonon-dispersion relation of YbPt$_5$B$_2$. In order to keep the number of parameters small, three essential Einstein modes are considered. Least-squares fits of Eq. (1) to the experimental data, together with the Sommerfeld term, reveal $\theta_D = 122.2$ K as well as $\theta_{E1} = 126$ K, $\theta_{E2} = 204$ K, and $\theta_{E3} = 497$ K with 5.85, 8 and 7.15 as appropriate weight coefficients, respectively [solid line, Fig. 5(a)]. Presumably, θ_{E3} corresponds to vibrations of lightweight boron. Both $\theta_D^{\rm LT}$ and θ_D values compare, when multiplying the latter one by $\sqrt[3]{N_{\rm atoms}}$ (i.e., $\theta_D\sqrt[3]{N_{\rm atoms}} = 244$ K). Comparing the Sommerfeld value γ with the DFT-derived DOS at $E = E_{\rm F}$ allows to estimate the electron-phonon enhancement factor $\lambda_{e,ph}$ as $\lambda_{e,ph} \sim 0.3$, referring to weak electron-phonon interactions in LuPt$_5$B$_2$.

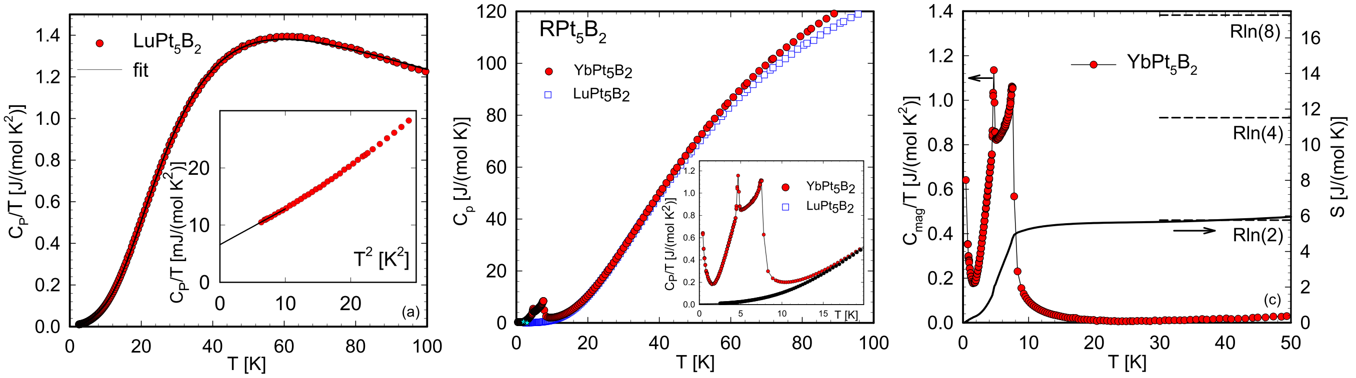

FIG. 5. (a) Temperature-dependent specific heat C_P of $LuPt_5B_2$ plotted as C_P/T vs T. The solid line corresponds to a least-squares fit discussed in detail in the text. The inset shows the data in a C_P/T vs T^2 representation; the solid line is a least-squares fit, $C_p = \gamma T + \beta T^3$, to reveal the Sommerfeld value γ and the low-temperature Debye temperature. (b) Temperature-dependent specific heat of $YbPt_5B_2$ compared with $LuPt_5B_2$ as C_P vs T. The inset shows low-temperature features of the measurement. (c) Temperature-dependent magnetic contribution to the specific heat, C_{mag}, of $YbPt_5B_2$ plotted as C_{mag}/T vs T and magnetic entropy S_{mag} vs T (right axis).

The temperature-dependent specific heat of $YbPt_5B_2$ is presented in Fig. 5(b), in comparison with the respective data of $LuPt_5B_2$; the difference between both curves in the HT range is obviously due to CEF contributions of excited doublets of $YbPt_5B_2$. The temperature-dependent magnetic contribution to the specific heat, C_{mag}, of $YbPt_5B_2$ was obtained by subtracting the temperature-dependent specific heat of nonmagnetic $LuPt_5B_2$, shown in Fig. 5(c) as C_{mag}/T vs T. The corresponding magnetic entropy, S_{mag} [Fig. 5(c), right axis], is derived from $S_{\text{mag}} = \int (C_{\text{mag}}/T)dT$. At low temperatures, C_{mag}/T of $YbPt_5B_2$ is characterized by a λ-like anomaly in the vicinity of $T_{\text{mag1}} \sim 7.8$ K, as well as by a peaklike structure around $T_{\text{mag2}} \sim 4.7$ K [compare Fig. 5(c)]. The anomaly at 7.8 K is typical for magnetic phase transitions of second order, while the peaklike anomaly is attributed to a first-order phase transition. For temperatures below 1.5 K, a substantial upturn of C_{mag}/T is obtained, which, at least partly, refers to Yb nuclear moment contributions, discussed below in more detail.

The magnetic phase transitions progressively release magnetic entropy; thus, $S_{\text{mag}}(T)$ exhibits a strong increase for $T < 8$ K, but reaches $R\ln 2$ only around 35 K (R is the gas constant). The fact that the magnetic entropy keeps quite constant from about 10 to roughly 50 K indicates that the CEF ground state of Yb is a doublet, while the excited levels are energetically well separated from the ground state (at least about 20 meV). This allows to conclude that magnetic ordering at low temperatures occurs in a pure doublet environment with negligible contributions from other levels. Furthermore, magnetic entropy data allow to set an upper limit of the Kondo temperature T_K of $YbPt_5B_2$. This is, because the Kondo effect spreads entropy to higher temperatures, above the ordering temperature T_{mag}. Following the procedure developed by Blanco *et al.* [51], T_K is given by

$$\frac{S_{\text{mag}}}{R} = \ln(1+\kappa) + \frac{T_K}{T_{\text{mag}}}\left(\frac{\kappa}{1+\kappa}\right), \quad \kappa = \exp\left(\frac{-T_K}{T_{\text{mag}}}\right). \tag{2}$$

Employing Eq. (2) to the experimentally obtained entropy data, $S_{\text{mag}}(T = T_N) \sim 0.86R\ln 2$, reveals $T_K < 7$ K. The upper limit is indicated because of unknown short-range order effects which are as well suited and expected to transfer entropy to above T_N.

The field response of the specific heat of $YbPt_5B_2$ is summarized in Fig. 6(a). Increasing magnetic fields shift the phase transition temperature towards lower values; they eventually become suppressed at sufficiently large magnetic fields, as expected for transitions of antiferromagnetic origin [see Fig. 6(a)]. The λ-like anomaly at $T_{\text{mag1}} \sim 7.8$ K is the least affected one by magnetic fields and is still clearly visible at 3 T. The height of the peak around $T_{\text{mag2}} \sim 4.7$ K, gradually decreases and simultaneously becomes broader with increasing fields, losing half of its height already at around 1 T. But, still for fields of 9 T, a small anomaly at T_{mag2} seems to be present which indicates that, for a specific relative orientation of the external magnetic field to the lattice axis, this transition is rather insensitive to the applied field.

Inspecting the field dependence of C_p/T at $T = 2.5$ K [Fig. 6(b)] reveals a significant initial increase, more than doubling the zero-field value (0.29 J/mol K^2) up to fields around 3 to 4 T and, finally above 4 T a continuous reduction. The initial increase refers to a transfer of entropy release towards lower temperatures, i.e., to a weakening of the AFM state, while the final shift of entropy transfer towards higher temperatures at above 4 T refers to a field-polarized paramagnetic state, i.e., the expected suppression of the antiferromagnetic state, which in the polycrystalline orientation average occurs at around 3 to 4 T.

Figure 6(c) illustrates the heat capacity obtained for the $4f$ part of $YbPt_5B_2$ and temperatures down to 150 mK. C_{4f} is derived from the measured data by subtracting the nuclear moment contribution of ^{171}Yb ($I = 1/2$, about 14%) and ^{173}Yb ($I = 5/2$, about 16%), since the phonon contribution to the measured data can be neglected in this temperature range (e.g., $C_{\text{ph}} \sim 0.8\%$ at $T = 1.5$ K). The nuclear moment contribution is estimated roughly via fitting the high-temperature tail of Schottky-like contributions to the specific heat. The resulting C_{4f}/T values of $YbPt_5B_2$ rise below 1.5 K, reaching a smooth maximum around 0.3 K; finally, a weak drop can be observed down to lowest temperatures. Note, data are collected from two independent measurements at different

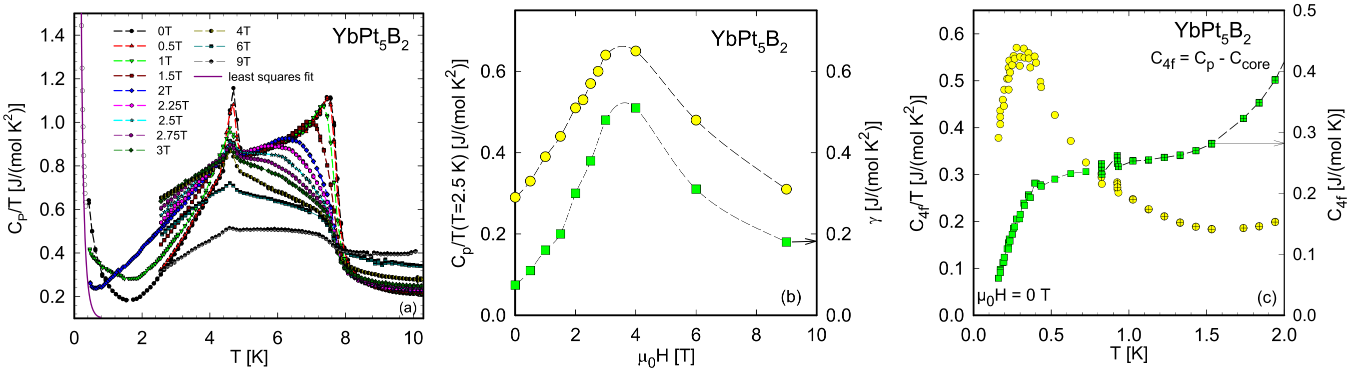

FIG. 6. (a) Temperature-dependent specific heat C_{P} of YbPt$_5$B$_2$ plotted as C_{P}/T vs T for various externally applied magnetic fields up to 9 T. The solid line to the low-temperature zero-field data accounts for the nuclear moment contribution of ^{171}Yb and ^{173}Yb atoms. (b) Field dependence of C_{P}/T taken at $T = 2.5$ K (left axis, yellow circles) and Sommerfeld value γ (right axis, green squares). The dashed line is a guide for the eyes. (c) Yb-4f contribution to the low-temperature specific heat of YbPt$_5$B$_2$, obtained after subtraction of the quadrupolar nuclear moment specific heat, plotted as C_{4f}/T vs T (left y axis, yellow circles) and C_{4f} vs T (right y axis, green squares).

temperature ranges. We do not expect that the C_{4f}/T maximum at $T \sim 0.3$ K indicates a magnetic phase transition, since C_{4f} vs T [right axis, Fig. 6(c)], does not reveal typical anomalies associated with phase transitions, referring to long-range magnetic order.

The magnetically ordered temperature range of YbPt$_5$B$_2$ can be analyzed in terms of an antiferromagnetic (AFM) spin-wave dispersion relation, i.e., $\omega = (\Delta^2 + D^2k^2)^{1/2}$, with Δ being the spin-wave gap and D is the spin-wave velocity. The resulting contribution to the specific heat, $C_{\mathrm{mag}}^{\mathrm{AFM}}$, can then be expressed as [52]

$$C_{\mathrm{mag}}^{\mathrm{AFM}} = B\Delta^{7/2}T^{1/2}\exp\left(-\Delta/T\right)\left[1+\frac{39}{20}\left(\frac{T}{\Delta}\right)+\frac{51}{32}\left(\frac{T}{\Delta}\right)^2\right], \tag{3}$$

where $B \propto 1/D^3$. In order to account for the experimentally obtained data, the background contribution due to electrons, $C_{\mathrm{el}} = \gamma T$, and the phonon contribution at low temperatures, $C_{\mathrm{ph}} = \beta T^3$, have to be taken into account, too. Employing both latter contributions, as well as Eq. (3), to the experimental data [Fig. 6(a)] reveals excellent agreement [solid lines, Fig. 7(a), exemplary for a few magnetic fields] for reasonable spin-wave gaps Δ and constants C, where $\Delta(\mu_0 H)$ is summarized in Fig. 7(b). For $\mu_0 H = 0$, the gap Δ below T_{mag2} is about 10 K; this value diminishes for increasing magnetic fields and seems to vanish almost linearly for fields above 12 T. This can be anticipated for the antiferromagnetic case [53,54], where the gap Δ is expected to modify according to $\Delta(\mu_0 H) = \Delta(\mu_0 H = 0) - \mu_{\mathrm{eff}} H_{\mathrm{eff}}$, where μ_{eff} is the effective magnetic moment and $H_{\mathrm{eff}} = \mu_0 H$-$H_{\mathrm{M}}$; the former is the externally applied magnetic field and the latter corresponds to the molecular field. The Sommerfeld parameter $\gamma(\mu_0 H)$ obtained from this fit is illustrated in Fig. 6(b), yielding $\gamma = 0.073$ J/mol K^2 for $\mu_0 H = 0$; this value increases continuously up to a maximum at $\mu_0 H = 4$ T, before decreasing to 0.18 J/mol K^2 at $\mu_0 H = 9$ T. This trend observed is in very good agreement with the $C_p/T(\mu_0 H)$ results taken at $T = 2.5$ K. To conclude, the very good agreement between the AFM model, Eq. (3), and the experimental data can be considered as a further proof of the AFM state present in YbPt$_5$B$_2$, particular in the AFM2 regime.

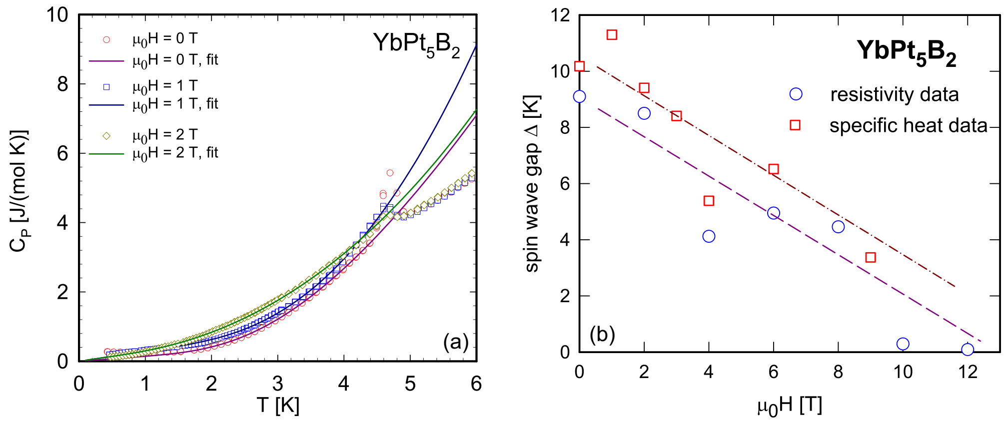

FIG. 7. (a) Temperature-dependent specific heat, C_{P}, of YbPt$_5$B$_2$ for several externally applied magnetic fields. The solid lines are least-squares fits according to Eq. (3) (b). Field-dependent spin-wave gap of YbPt$_5$B$_2$ of the low-temperature phase obtained from specific-heat and electrical resistivity data.

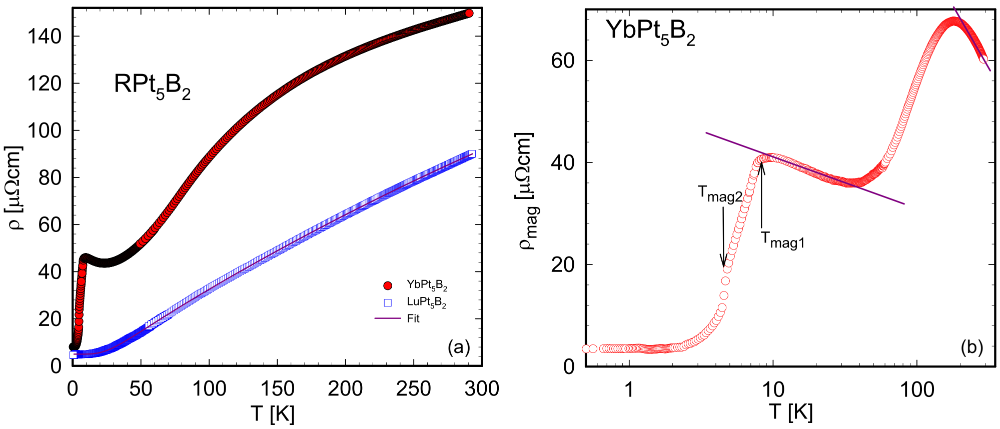

FIG. 8. (a) Temperature-dependent electrical resistivity, ρ, of YbPt$_5$B$_2$ compared to that of LuPt$_5$B$_2$. The solid line corresponds to a least-squares fit according to Eq. (4). (b) Temperature-dependent magnetic contribution to the electrical resistivity, ρ_{mag}, of YbPt$_5$B$_2$ plotted on a logarithmic temperature scale.

4. Electrical resistivity

The temperature-dependent electrical resistivity, ρ, of YbPt$_5$B$_2$ and its nonmagnetic counterpart, LuPt$_5$B$_2$, is plotted in Fig. 8(a). LuPt$_5$B$_2$ behaves metallic in the entire temperature range, showing no anomalies down to the lowest temperatures (0.3 K). The experimental data of the latter can be analyzed in terms of a temperature-independent residual resistivity, ρ_0, and a temperature-dependent electron-phonon contribution, ρ_{ph} [Eq. (4)]:

$$\begin{aligned} \rho(T) &= \rho_0 + \rho_{\mathrm{ph}}(T), \\ \rho_{\mathrm{ph}}(T) &= c_0\left(\frac{T}{\Theta_D}\right)^5 \int_0^{\Theta_D/T} \frac{x^5\,dx}{(e^x-1)(1-e^{-x})}, \end{aligned} \tag{4}$$

$\rho_{\mathrm{ph}}(T)$ is commonly described employing the Bloch-Grüneisen model [Eq. (4)], which accounts for the interaction of electrons with thermally excited phonons. c_0 is a material-dependent, temperature-independent electron-phonon interaction constant. In order to adapt to the real experimental data, a parallel resistivity model is assumed, with an upper limit of the resistivity for $T \to \infty$. This ansatz provides an appropriate slight curvature of $\rho(T)$, which is absent in the simple Bloch-Grüneisen formula ($\rho \propto T$, $T \gtrsim \theta_D$). A least-squares fit yields $\rho_0 = 5\ \mu\Omega$ cm and $\theta_{\mathrm{D}} = 155$ K, a value which is often associated with the Debye temperature. Magnetic fields affect the resistivity of LuPt$_2$B$_5$ only very weakly, resulting in a minor increase of $\rho(T)$ in the entire temperature range.

With decreasing temperature, $\rho(T)$ of YbPt$_5$B$_2$ decreases, exhibiting a strong curvature as a consequence of conduction electron scattering on the magnetic moments of Yb. The latter is modified by CEF effects in the context of Kondo-type interactions. The decrease of $\rho(T)$ is followed by a Kondo-driven increase below 20 K. Below about 8 K, $\rho(T)$ drops substantially, indicating a magnetic phase transition, in perfect accordance with the susceptibility and heat-capacity data. Another sharp drop of $\rho(T)$ traces a second magnetic phase transition, around $T_{\mathrm{mag2}} \sim 4.7$ K [compare also Fig. 8(b)]. Finally, a residual resistivity $\rho_0 = 5\ \mu\Omega$ cm is attained, marking the very good sample quality of the specimen under investigation.

Figure 8(b) reveals the temperature-dependent magnetic contribution to the electrical resistivity, ρ_{mag}, of YbPt$_5$B$_2$, derived by subtracting $\rho(T)$ of LuPt$_5$B$_2$ from $\rho(T)$ of YbPt$_5$B$_2$. The logarithmic temperature scale proves two negative logarithmic temperature ranges in $\rho_{\mathrm{mag}}(T)$ as a consequence of Kondo interaction in the presence of strong CEF splitting [55]. While the lower of these domains points to the Kondo effect in the CEF ground state, the upper one refers to Kondo interaction in the overall split system. The two magnetic phase transitions are prominently rendered in this semilogarithmic plot too.

To better figure out details of both magnetic phase transitions, besides the experimental resistivity data, $d\rho/dT$ is added as a solid line to Fig. 9(a), referring to the right axis. $d\rho/dT$ exhibits a steplike change around 7.8 K and a peaklike anomaly at 4.6 K, in excellent agreement with the specific-heat data.

To quantitatively account for the magnetically ordered temperature range, besides ρ_0 and a Fermi-liquid contribution, $\rho_{\mathrm{el}} = \mathrm{A}T^2$, the spin-wave model discussed above, can be employed too. Following the procedure developed by Continentino *et al.* [52], the spin-wave dependent resistivity, $\rho_{\mathrm{mag}}^{\mathrm{AFM}}$, can be stated as

$$\rho^{\mathrm{AFM}} = C\Delta^{3/2}T^{1/2}\exp(-\Delta/T)\left[1 + \frac{2}{3}\left(\frac{T}{\Delta}\right) + \frac{2}{15}\left(\frac{T}{\Delta}\right)^2\right]. \tag{5}$$

Again, C is a constant, with $C \propto 1/D^3$. Moreover, $C \propto 1/\Gamma^3$, where Γ is an effective magnetic coupling between the Yb ions [52]. Least-squares fits in the low-temperature domain have been performed and results are shown as solid lines in Fig. 9(a), revealing very good agreement with the experimental data, with $\Delta_{\mathrm{LT}} = 8.5$ K. The absolute value appears to be quite reasonable with respect to the respective magnetic phase transition temperature and compares well with results from specific heat. The Fermi-liquid prefactor A, obtained additionally from the present least-square fit, allows to rank YbPt$_5$B$_2$ within the large family of correlated electron systems, when additionally considering the Sommerfeld value γ, as acquired in the previous paragraph. This is done

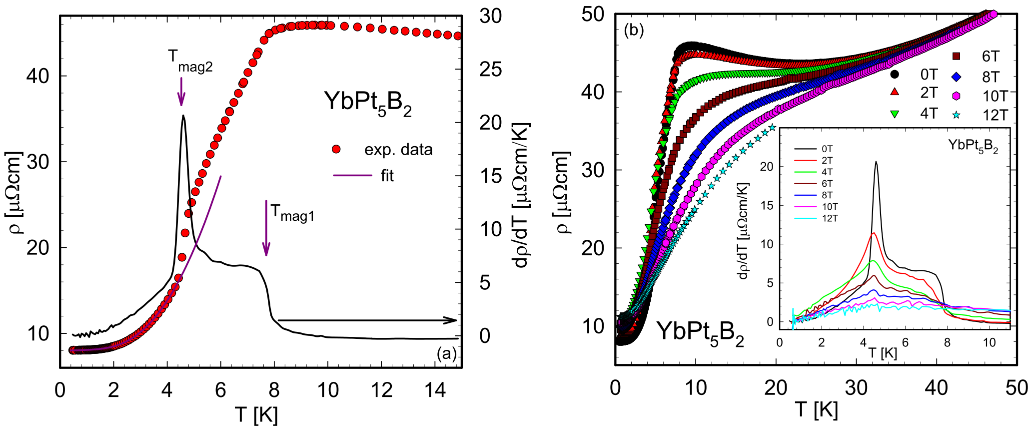

FIG. 9. (a) Low-temperature electrical resistivity, ρ, of $YbPt_5B_2$. The purple solid line is a least-squares fit according to Eq. (5). The black solid line is the derivative $d\rho/dT$ of $YbPt_5B_2$, referring to the right axis. (b) Temperature-dependent electrical resistivity, ρ, of $YbPt_5B_2$ at different magnetic fields. The inset exhibits the field-dependent evolution of $d\rho/dT$ of $YbPt_5B_2$ for magnetic fields up to 12 T.

employing the Kadowaki-Woods (KW) relation [56], revealing for Ce or Yb compounds with small ground-state degeneracy of the magnetic ions (i.e., Ce^{3+} and Yb^{3+}) a universal relation, $R_{KW} = A/\gamma^2 \sim 1.0 \times 10^{-5}$ $\mu\Omega$ cm (mol K/mJ)^2. This value is, at least, one order of magnitude above that of common d-band metals. Taking into account the least-squares fit data of $YbPt_5B_2$ ($A = 0.061$ $\mu\Omega$ cm K^{-2}, $\gamma = 71$ mJ/mol K^2 at zero magnetic field) reveals $R_{KW} = A/\gamma^2 = 1.22 \times 10^{-5}$ $\mu\Omega$ cm (mol K/mJ)^2, a value which nicely matches the Kadowaki-Woods plot established for many of Ce- and Yb-based heavy-fermion compounds.

The response of $YbPt_5B_2$ to the application of externally applied magnetic fields is summarized in Fig. 9(b). At temperatures above the magnetic phase transitions, $\rho(T)$ decreases upon the application of a magnetic field, referring to a negative magnetoresistance. Magnetic fluctuations of the Yb^{3+} moment become suppressed by magnetic fields, hence the resistivity decreases. As is obvious from Fig. 9(b), the suppression is largest in the proximity of the phase transitions. Least-squares fits for the various magnetic field data have been carried out and results concerning the spin-wave gap are collected in Fig. 7(b) too, revealing an almost linear decrease of Δ with increasing field values, in rather good agreement with the respective C_p $(T, \mu_0 H)$ data.

The inset of Fig. 9(b) summarizes the temperature derivatives $d\rho/dT(\mu_0 H)$ of $YbPt_5B_2$ for various values of applied magnetic fields. Since $d\rho/dT$ of magnetic materials mirrors specific-heat data of the same material [57] even in applied magnetic fields, field-driven changes of phase transitions can be resolved and compared with the respective heat-capacity data. In fact, the inset of Fig. 9(b) compares well with Fig. 6(a), revealing in both cases a decrease of the magnetic phase transition temperature, as well as a rapid suppression of the height of the respective anomalies

5. Magnetoresistance

The temperature-dependent magnetoresistance of $YbPt_5B_2$, defined as $\delta\rho = \rho(\mu_0 H, T) - \rho(\mu_0 H = 0, T)$, is shown for various magnetic fields in Fig. 10(a). For all fields, a distinct minimum is present around $T = 8$ K, followed by an anomaly below 5 K, which becomes smeared out as the field values increase. While the former is related to T_{mag1}, the latter hints at T_{mag2}. In the elevated temperature range, $\delta\rho$ can be accounted for by a behavior proportional to $1/[(T/T_{mag}) - 1]^2$, in accordance with predictions of Yamada and Takada [58]. In addition, $\delta\rho(T)$ is characterized by a crossover from negative (high temperatures) to positive (low temperatures) values at a temperature T_{cr}. The field dependence of T_{cr} is displayed in the inset of Fig. 10(a), revealing an initial decrease, followed by a saturation behavior. Above T_{cr}, the negative values of $\delta\rho$ can be understood from the suppression of spin fluctuations by external magnetic fields and thus by a reduction of the interaction of electrons with the Yb magnetic moments, resulting in an increase of conductivity. Below T_{cr}, $\delta\rho$ rises with magnetic fields, presumably due to a decrease of the gap energy Δ [54] [compare Fig. 7(b)]. As a consequence, more magnons are excited; thus, an increase of the electron-magnon scattering takes place and the resistivity increases. Contributions of the classical magnetoresistance may slightly enhance this effect.

The isothermal magnetoresistance, $\Delta\rho/\rho = [\rho(\mu_0 H, T) - \rho(\mu_0 H = 0, T)]/\rho(\mu_0 H = 0, T)$ of $YbPt_5B_2$ [Fig. 10(b)] initially exhibits a slight positive increase with rising fields for temperatures below $T_{mag2} = 4.7$ K. For the isothermal run at $T = 0.6$ K, a distinct change of the slope of $\Delta\rho/\rho(\mu_0 H)$ around 1.9 T is obtained, which likely traces a reorientation of the zero field magnetic moment structure. At fields around 3 T, a smooth maximum is present, while around 5.5 T another clear-cut change of the slope of $\Delta\rho/\rho(\mu_0 H)$ is observed. The initial positive magnetoresistance is a typical feature of an antiferromagnetic ground state [58], where $\Delta\rho/\rho$ rises, until—in general—a field-induced ferromagnetic regime is reached at a critical field value, where $\Delta\rho/\rho$ starts to decrease. As a result, a more or less pronounced maximum is formed. Theoretically, positive values of $\Delta\rho/\rho$ of AFM systems are expected for fields parallel to the sublattice magnetization, while $\Delta\rho/\rho$ keeps constant for fields perpendicular to the spin arrangement [58]. Hence, below

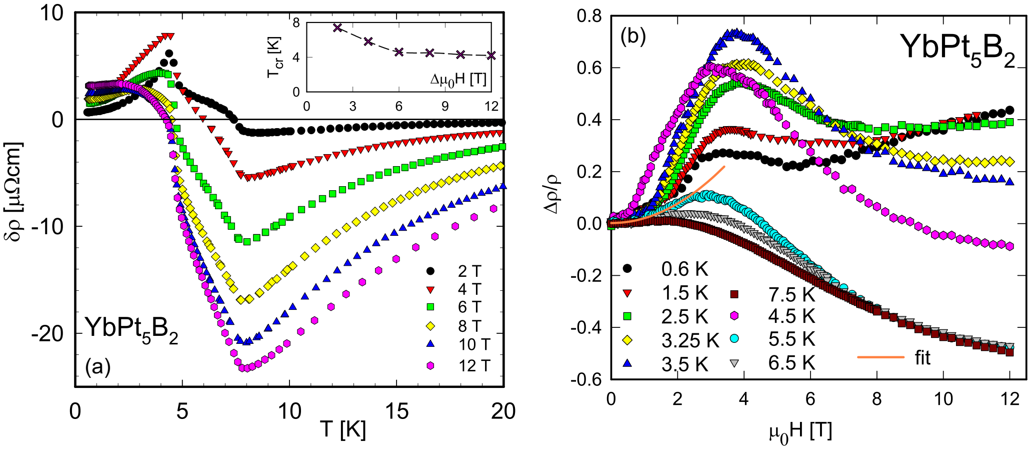

FIG. 10. (a) Temperature-dependent magnetoresistance $\delta\rho = \rho(\mu_0 H, T) - \rho(\mu_0 H = 0, T)$ of YbPt$_5$B$_2$ for various values of the externally applied magnetic field. The inset shows the field dependence of the crossover temperature T_{cr}. (b) Field-dependent magnetoresistance, $\Delta\rho/\rho$, of YbPt$_5$B$_2$ at different temperatures. The solid orange line is a fit to the $T = 5.5$ K run based on a $\Delta\rho/\rho \propto (\mu_0 H)^2$ behavior.

the critical field, a polycrystalline sample will always exhibit positive $\Delta\rho/\rho$ values. Besides the expected decrease of $\Delta\rho/\rho$ at larger magnetic fields due to the suppression of magnetic fluctuations, a positive contribution to $\Delta\rho/\rho$ might become obvious, because of the classical magnetoresistance. The latter can be non-negligible in YbPt$_5$B$_2$ at low temperatures, since the respective residual resistivity is low. Both contributions may overlay, forming an anomaly, which should not be confused with a field-induced phase transition.

As the temperature is increased, the low-field anomaly shifts to even lower field values (0.75 T at 4.5 K, Fig. 10), while the maximum increases and becomes more pronounced. For isothermal field runs at $T_{\mathrm{mag1}} < T < T_{\mathrm{mag2}}$, qualitatively and quantitatively different features of $\Delta\rho/\rho$ are evident from Fig. 10. Again, positive $\Delta\rho/\rho$ values are revealed initially, followed by a shallow maximum; above this, fairly large negative $\Delta\rho/\rho$ values can be noticed, about 50% for fields of 12 T. The faint maxima shift to lower fields, from 2.9 T ($T = 5.5$ K) to 1.6 T ($T = 7.5$ K). Overall, these features are again reminiscent of a classical AFM, with the maxima referring to the critical fields, where AFM turns over into a field-induced FM state and FM fluctuations become suppressed for further increasing fields. The s-like shape of $\Delta\rho/\rho(\mu_0 H)$ in the high-field limit, as well as the very large absolute values, are in accordance with expectations of a Kondo scenario, as pointed out in detail by Schlottmann *et al.* [59]. To corroborate the AFM scenario from a more quantitative point of view, a behavior of $\Delta\rho/\rho \propto (\mu_0 H)^2$ below the critical field is expected [57], and in fact it is observed from the present experiments (as an example, compare the orange solid line in Fig. 10 for the $T = 5.5$ K run).

6. Thermal expansion and magnetostriction

The temperature-dependent thermal expansion $\Delta l/l_0$ of YbPt$_5$B$_2$ for various values of applied magnetic fields is shown in Figs. 11(a) and 11(b). This quantity consists of contributions from electrons, phonons, and magnetic moments and is directly related to the heat capacity via the Grüneisen relation. $\Delta l/l_0$ is set to zero at 2.8 K (except for the 9 T run). Distinct anomalies are present at both magnetic phase transition temperatures, T_{mag1} and T_{mag2}, which become more pronounced employing a first derivative of these data with respect to temperature [examples are shown in the inset of Fig. 11(b)]. In the paramagnetic temperature range [Fig. 11(b)], $\Delta l/l_0$ exhibits a positive slope, i.e., the thermal expansion coefficient α is strongly temperature dependent, ranging from $\alpha = 1 \times 10^{-6}$ at $T = 20$ K to $\alpha = 8 \times 10^{-6}$ at $T = 300$ K. CEF effects presumably contribute to this observation.

For $\mu_0 H = 3.5$ T, the initially positive thermal expansion changes sign around 5.5 K, after passing a maximum at 4.2 K. The kinklike structure at $T = 7.5$ K marks the phase transition at T_{mag1}. Increasing the magnetic field to $\mu_0 H = 4$ T reveals a change of the regime towards entirely negative thermal expansion data; a slight anomaly around 7.5 K might be indicative of the phase transition at T_{mag1}. The 9 T run shows large negative values with increasing temperature. An anomaly tracing the phase transition seems to be no longer present. Besides the magnetic phase transitions detected from $\Delta l/l_0$ data, the crossover from positive to negative thermal expansion with increasing fields is quite remarkable.

The field-dependent magnetostriction, $\lambda_{\mathrm{ms}} = \Delta l/l_0(\mu_0 H)$ ($T =$ const), of YbPt$_5$B$_2$ is positive at all temperatures as summarized in Fig. 11(c). Except for the 10 K run ($T > T_{\mathrm{mag1}}$), field-induced phase transitions are obvious from kinks in $\lambda_{\mathrm{ms}}(\mu_0 H)$, which become more pronounced and which shift to larger field values as the temperature is decreased. This feature is more obvious from a first derivative with respect to the applied magnetic field, $d\lambda_{\mathrm{ms}}/dH$, as shown in Fig. 11(d). As the temperature drops below 4.8 K, a second field-induced phase transition is present, in perfect agreement with the previously discussed bulk properties (susceptibility, resistivity, and specific heat).

Magnetostriction of YbPt$_5$B$_2$ is present in both the ordered and the paramagnetic temperature range. Its magnitude is about 5 to 10 times larger than the magnetostriction of Ni or Fe, but about 5 times smaller than that of Terfenol (TbFe$_2$) [60]. Simple magnetic materials might exhibit either positive or negative values; its origin is, besides microstructural

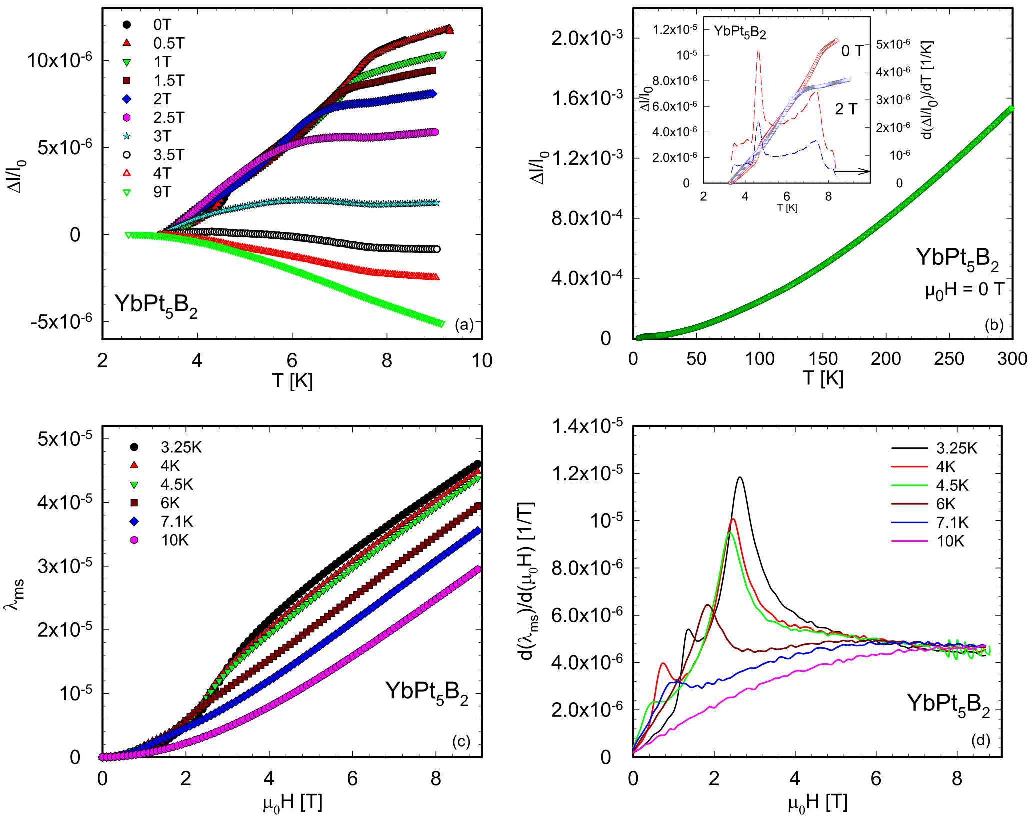

FIG. 11. (a) Low-temperature dependent thermal expansion $\Delta l/l_0$ of $YbPt_5B_2$ for various values of applied magnetic fields. (b) Thermal expansion of $YbPt_5B_2$ from 3 to 300 K. The inset shows examples of $\Delta l/l_0$ (left axis) and of the first derivative of $\Delta l/l_0$ with respect to temperature (right axis). (c) Field-dependent magnetostriction λ_{ms} of $YbPt_5B_2$ at different temperatures. (d) Derivative of the magnetostriction, $d\lambda_{ms}/d(\mu_0 H)$, of $YbPt_5B_2$ at different temperatures.

features, primarily a result of the spin-orbit coupling of magnetic moments. Crystalline electric-field splitting might contribute to the magnetostriction too.

7. *Magnetic phase diagram*

To construct the magnetic phase diagram for $YbPt_5B_2$, the temperature dependence of upper and lower transition magnetic fields was built using the magnetoresistance and magnetostriction data. The procedure which was employed to achieve these values is described in Fig. 12(a), using 3.25 K data as an example. Since polycrystalline samples were used in this study, field-induced phase transitions obtained are representing an average over the respective values in the principal directions of the monoclinic unit cell. Preferred orientation of grains have not been observed from x-ray diffraction pattern.

The analysis of magnetostriction data is rather straightforward; higher and lower temperature peaks in the derivative of

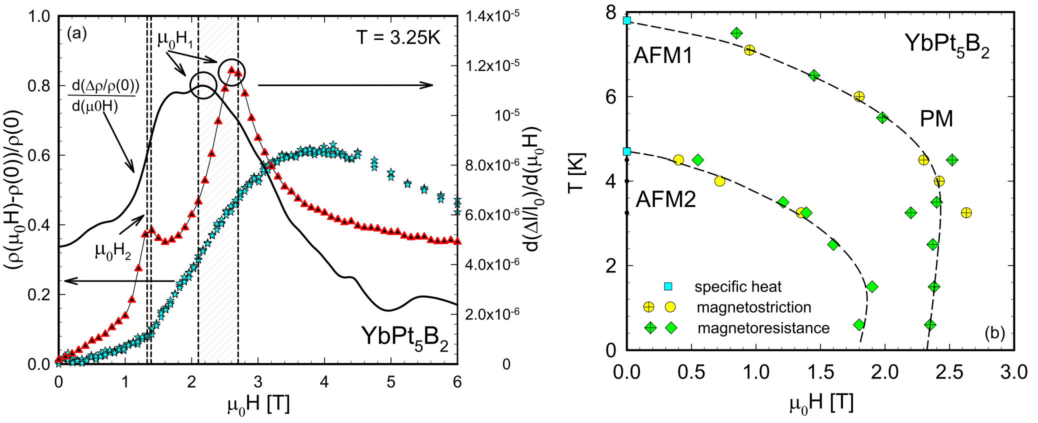

FIG. 12. (a) Illustration of how characteristic magnetic fields, using magnetostriction and magnetoresistance data, are obtained. (b) Tentative magnetic phase diagram of $YbPt_5B_2$.

the longitudinal magnetostriction of $YbPt_5B_2$, λ'_{ms}, are associated with μ_0H_1 and μ_0H_2, respectively. To extract the analogs' values from magnetoresistance data, the derivative $(\Delta\rho/\rho)' = d(\Delta\rho/\rho)/d(\mu_0H)$ for the appropriate temperature data has to be taken first. The medium value of the upturn (corresponding to the visible kink in the magnetoresistance data) is associated with μ_0H_2. A zero in $(\Delta\rho/\rho)''$, that corresponds to the peak in $(\Delta\rho/\rho)'$ is associated with μ_0H_1. Summarizing the data received via both methods, a tentative magnetic phase diagram of $YbPt_5B_2$ was constructed (Fig. 12).

IV. SUMMARY

Ternary {Yb,Lu}Pt_5B_2 borides have been prepared and low-temperature properties have been studied. YPt_5B_2 and $LuPt_5B_2$ were found to be isostructural. The layered $YbPt_5B_2$ structure is built of $CeCo_3B_2$-type related fragments, which are oriented perpendicularly to each other along the longer direction of the unit cell. The structure shows an arrangement of structural units similar to that observed in borides from the homologous series of the $CeCo_3B_2$ type, $NaPt_3B$ [19] and $SrPd_4B$ [29]. Both $LuPt_5B_2$ and YPt_5B_2 are characterized by metallic resistivity features.

$YbPt_5B_2$, as expected for intermetallic compounds with Yb, behaves as a paramagnetic material in the high-temperature region, exhibiting an effective magnetic moment near that of Yb^{3+} (Yb $4f^{13}$). For temperatures below 8 K, $YbPt_5B_2$ undergoes at least two magnetic phase transitions, very likely of antiferromagnetic origin. The transition at higher temperature is of a second-order type, while that at lower temperature is of first order. Magnetism in the low-temperature range is modified by the presence of Kondo interactions ($T_K = 7$ K), as well as by crystalline electric-field effects, causing a lifting of the eightfold degenerate ground state ($j = 7/2$) into four doublets. As a result, the magnetic entropy expected for Yb^{3+} ($S_{mag} = R\ln 8$) is not recovered in the temperature range up to 100 K. The presence of the Kondo effect and CEF splitting is characteristically revealed from the magnetic contribution to the temperature-dependent electrical resistivity, ρ_{mag}, by negative logarithmic ranges, as well as by an archetypal maximum in $\rho_{mag}(T)$. Combining the Sommerfeld value γ and the Fermi-liquid prefactor A of the resistive T^2 behavior, i.e., $R_{KW} = A/\gamma^2 = 1.22 \times 10^{-5}$ $\mu\Omega$ cm $(\text{mol K/mJ})^2$, reveals excellent agreement with the Kadowaki-Woods relation of heavy-fermion compounds. Upon the application of magnetic fields, and $T < T_{mag2}$, two field-induced phase transitions are observed at around 1.9 and 2.4 T. For $T_{mag2} < T < T_{mag1}$ one field-induced phase transition is obtained, as obvious from isothermal magnetoresistance and magnetostriction data. ^{171}Yb and ^{173}Yb are responsible for huge contributions to the specific of $YbPt_5B_2$ at very low temperatures.

ACKNOWLEDGMENTS

Research supported by Austrian Science Fund (FWF) Grant No. P 31979. A.S. was supported by the JSPS program for Postdoctoral Fellow Research Abroad.

[1] J. Nagamatsu, N. Nakagawa, T. Muranaka, Y. Zenitani, and J. Akimitsu, Superconductivity at 39 K in magnesium diboride, Nature (London) **410**, 63 (2001).

[2] H. Knoch, Borides, in *Concise Encyclopedia of Advanced Ceramic Materials*, edited by R. J. Brook (Pergamon Press, Oxford), pp. 35–38 (1991).

[3] T. Mori, Rare earth higher borides, in *Handbook on the Physics and Chemistry of Rare Earths*, edited by J.-C. G. Bünzli and V. K. Pecharsky (Elsevier, Amsterdam, 2020), Vol. 58, Chap. 316, pp. 39–154.

[4] T. Komatsubara, N. Sato, S. Kuni, I. Oguro, Y. Furukawa, Y. Onuki, and T. Kasuya, Dense Kondo behavior in CeB_6 and its alloys, J. Magn. Magn Mater. **31–34**, 368 (1983).

[5] K. Flachbart, S. Gabani, K. Gloos, M. Meissner, M. Opel, Y. Paderno, V. Pavlık, P. Samuely, E. Schuberth, N. Shitsevalova, K. Siemensmeyer, and P. Szabo, Low temperature properties and superconductivity of LuB_{12}, J. Low Temp. Phys **140**, 339 (2005).

[6] S. K. Dhar, S. K. Malik, and R. Vijayaraghavan, Strong itinerant magnetism in ternary boride $CeRh_3B_2$, J. Phys. C **14**, L321 (1981).

[7] S. Nie, Y. Sun, F. B. Prinz, Z. Wang, H. Weng, Z. Fang, and X. Dai, Magnetic Semimetals and Quantized Anomalous Hall Effect in EuB_6, Phys. Rev. Lett. **124**, 076403 (2020).

[8] D. Kim, J. Xia, and Z. Fisk, Topological surface state in the Kondo insulator samarium hexaboride, Nat. Mater. **13**, 466 (2014).

[9] F. Iga, N. Shimizu, and T. Takabatake, Single crystal growth and physical properties of Kondo insulator YbB_{12}, J. Magn. Magn. Mater. **177-181**, 337 (1998).

[10] K. Hagiwara, Y. Ohtsubo, M. Matsunami, S. I. Ideta, K. Tanaka, H. Miyazaki, J. E. Rault, P. Le Fèvre, F. Bertran, A. Taleb-Ibrahimi, R. Yukawa, M. Kobayashi, K. Horiba, H. Kumigashira, K. Sumida, T. Okuda, F. Iga, and S. I. Kimura, Surface Kondo effect and non-trivial metallic state of the Kondo insulator YbB_{12}, Nat. Commun. **7**, 12690 (2016).

[11] L. C. Gupta, Quaternary borocarbide superconductors, Philos. Mag. B **77**, 717 (1998).

[12] P. Rogl, Existence and crystal chemistry of borides, in *Inorganic Reactions and Methods*, edited by J. J. Zuckerman (VCH Publishers, Weinheim, Germany, 1991), Vol. 13, Chap. 6, pp. 85–167.

[13] Yu. B. Kuz'ma, *Crystal Chemistry of Borides* (Vyshcha Shkola, Lvov, 1983), p. 164.

[14] E. Parthé and B. Chabot, Crystal structures and crystal chemistry of ternary rare earth-transition metal borides, silicides and homologues, in *Handbook on the Physics and Chemistry of Rare Earths*, edited by K. Gschneidner, Jr. and L. Eyring (Elsevier, Amsterdam, 1984), Vol. 6, Chap. 48, pp. 113–334.

[15] P. S. Salamakha, O. L. Sologub, C. Rizzoli, J. R. Hester, J. Stepien-Damm, A. P. Gonçalves, E. B. Lopes, and M. Almeida, Ternary RPt_4B (R = La, Ce, Pr, Nd) Compounds; structural and physical characterisation, Intermetallics **12**, 1325 (2004).

[16] O. Sologub, C. Rizzoli, P. Salamakha, and H. Ipser, Structural investigation of ternary RIr_3B_2 compounds (R = Ce and Pr), J. Alloys Comp. **360**, 127 (2003).

[17] P. Salamakha, O. Sologub, A. P. Gonçalves, and M. Almeida, $Ce_2Ir_5B_2$, a new structure type of ternary borides, J. Alloys Comp. **360**, 131 (2003).

[18] O. L. Sologub, L. P. Salamakha, H. Noël, T. Roisnel, and A. P. Gonçalves, $La_3Ru_8B_8$ and $Y_3Os_8B_6$, new members of a homologous series $RE(An)_nM_{3n-1}B_{2n}$, J. Solid State Chem. **180**, 2740 (2007).

[19] R. N. Shelton, Superconductivity and crystal structure of a new class of ternary platinum borides, J. Less-Common Met. **62**, 191 (1978).

[20] R. Mirgel and W. Jung, The ternary alkali metal platinum borides $LiPt_3B$, $NaPt_3B_{1+x}$ and $Na_3Pt_9B_5$ - New structure variants of the $CeCo_3B_2$ type, J. Less-Common Met. **144**, 87 (1988).

[21] L. Salamakha, E. Bauer, G. Hilscher, H. Michor, O. Sologub, P. Rogl, and G. Giester, Structural and physical properties diversity of new $CaCu_5$-type related europium platinum borides, Inorg. Chem. **52**, 4185 (2013).

[22] F. Stegemann, J. Stahl, M. Bartsch, H. Zacharias, D. Johrendt, and O. Janka, Temperature induced valence phase transition in intermediate-valent $YbPd_2Al_3$, Chem. Sci. **10**, 11086 (2019).

[23] R. Pöttgen, T. Jüstel, and C. A. Strassert, *Rare Earth Chemistry* (DeGruyter, Berlin, 2020), p. 654.

[24] J. L. Sarrao, C. D. Immer, Z. Fisk, C. H. Booth, E. Figueroa, J. M. Lawrence, R. Modler, A. L. Cornelius, M. F. Hundley, G. H. Kwei, J. D. Thompson, and F. Bridges, Physical properties of $YbXCu_4$ (X = Ag, Au, Cd, Mg, Tl, and Zn) compounds, Phys. Rev. B **59**, 6855 (1999).

[25] R. Pöttgen, D. Johrendt, and D. Kussmann, Structure-property relaternary quiatomic YbTX intermetallics, in *Handbook on the Physics and Chemistry of Rare Earths*, edited by K. Gschneidner, Jr. and L. Eyring (Elsevier, Amsterdam, 2001), Vol. 32, Chap. 207, p. 453.

[26] O. Sichevych, Y. Prots, Y. Utsumi, L. Akselrud, M. Schmidt, U. Burkhardt, M. Coduri, W. Schnelle, M. Bobnar, Y.-T. Wang, Y.-H. Wu, K.-D. Tsuei, L. H. Tjeng, and Y. Grin, Intermediate-valence ytterbium compound $Yb_4Ga_{24}Pt_9$: Synthesis, crystal structure, and physical properties, Inorg. Chem. **56**, 9343 (2017).

[27] S. Nakamura, S. Toyoshima, N. Kabeya, K. Katoh, T. Nojima, and A. Ochiai, Low-temperature properties of the $S = 1/2$ spin system Yb_3Ru_4Al with a distorted Kagome lattice structure, Phys. Rev. B **91**, 214426 (2015).

[28] A. He, E. L. Kunz Wille, L. M. Moreau, S. M. Thomas, J. M. Lawrence, E. D. Bauer, C. H. Booth, and S. M. Kauzlarich, Intermediate Yb valence in the Zintl phases $Yb_{14}MSb_{11}$ (M = Zn, Mn, Mg): XANES, magnetism, and heat capacity, Phys. Rev. Mater. **4**, 114407 (2020).

[29] S. Nakatsuji, K. Kuga, Y. Machida, T. Tayama, T. Sakakibara, Y. Karaki, H. Ishimoto, S. Yonezawa, Y. Maeno, E. Pearson, G. G. Lonzarich, L. Balicas, H. Lee, and Z. Fisk, Superconductivity and quantum criticality in the heavy-fermion system ß-$YbAlB_4$, Nature Phys. **4**, 603 (2008).

[30] A. Svane, W. M. Temmerman, Z. Szotek, L. Petit, P. Strange, and H. Winter, Ab initio theory of valency in ytterbium compounds, Phys. Rev. B **62**, 13394 (2000).

[31] E. Schuberth, M. Tippmann, L. Steinke, S. Lausberg, A. Steppke, M. Brando, C. Krellner, C. Geibel, R. Yu, Q. Si, and F. Steglich, Emergence of superconductivity in the canonical heavy-electron metal $YbRh_2Si_2$, Science **351**, 485 (2016).

[32] M. S. Kim, M. C. Bennett, D. A. Sokolov, M. C. Aronson, J. N. Millican, J. Y. Chan, Q. Huang, Y. Chen, and J. W. Lynn, Synthesis and study of the heavy-fermion compound Yb_5Pt_9, Phys. Rev. B **74**, 224431 (2006).

[33] R. T. Khan, F. Kneidinger, G. Hilscher, A. Sidorenko, O. Sologub, H. Michor, E. Bauer, P. Rogl, and G. Giester, Thermal, magnetic and electronic properties of non-centrosymmetric $YbPt_2B$, J. Phys.: Condens. Matter **27**, 146001 (2015).

[34] L. Salamakha, H. Michor, H. Müller, E. Bauer, O. Sologub, B. Stöger, and P. Rogl, Magnetic instabilities and Kondo lattice behaviour of $YbPt_5B_2$, a new boride compound, in *The International Conference on Strongly Correlated Electron Systems, SCES 2020/21*, Guarujá, SP, Brazil, September 27–October 2, 2021, Book of Abstracts.

[35] Nonius Kappa CCD, Program Packages COLLECT, DENZO, SCALEPACK, SORTAV, Nonius Delft, The Netherlands.

[36] See Supplemental Material at http://link.aps.org/supplemental/10.1103/PhysRevB.105.205112 for more details regarding the crystal and electronic structures of $YbPt_5B_2$, $LuPt_5B_2$ and the Brillouin zone of $LuPt_5B_2$.

[37] L. J. Farrugia, WINGX and ORTEP for Windows: An update, Appl. Crystallogr. **45**, 849 (2012).

[38] J. Rodriguez-Carvajal, Recent advances in magnetic structure determination by neutron powder diffraction, Physica B **192**, 55 (1993).

[39] T. Roisnel and J. Rodriguez-Carvajal, WinPLOTR: A Windows tool for powder diffraction patterns analysis, Material Science Forum, *Proceedings of the 7th European Powder Diffraction Conference (EPDIC 7)*, edited by R. Delhez and E. J. Mittenmeijer (Trans. Tech. Publications Ltd., 2001), Vols. 378–381, p. 118.

[40] G. Kresse and J. Furthmüller, Efficiency of ab-initio total energy calculations for metals and semiconductors using a plane-wave basis set, Comput. Mater. Sci. **6**, 15 (1996).

[41] G. Kresse and J. Furthmüller, Efficient iterative schemes for *ab initio* total-energy calculations using a plane-wave basis set, Phys. Rev. B **54**, 11169 (1996).

[42] P. E. Blöchl, Projector augmented-wave method, Phys. Rev. B **50**, 17953 (1994).

[43] G. Kresse and D. Joubert, From ultrasoft pseudopotentials to the projector augmented-wave method, Phys. Rev. B **59**, 1758 (1999).

[44] J. P. Perdew and Y. Wang, Accurate and simple analytic representation of the electron-gas correlation energy, Phys. Rev. B **45**, 13244 (1992).

[45] M. Rotter, H. Müller, E. Gratz, M. Doerr, and M. Loewenhaupt, A miniature capacitance dilatometer for thermal expansion and magnetostriction, Rev. Sci. Instrum. **69**, 2742 (1998).

[46] R. Gumeniuk, M. Schmitt, W. Schnelle, U. Burkhardt, H. Rosner, and A. Leithe-Jasper, $SrPd_4B$ and $BaPd_4B$: New type of crystal structure and physical properties, Z. Anorg. Allg. Chem. **636**, 954 (2010).

[47] J. L. C. Daams, J. R. Rodgers, and P. Villars, Typical interatomic distances: Metals and alloys, in *International Tables for Crystallography, Mathematical, Physical and Chemical Tables*,

Vol. C (Kluwer Academic Publishers, Dordrecht, Boston, London, 2004), p. 774.

[48] M. Ellner, J. Grin, P. Fischer, and P. Rogl, Roentgen- und Neutronenbeugungsuntersuchungen der Struktur von $\mathrm{Pt_3B_2}$, Zeitschrift f. Metallkunde **84**, 788 (1993).

[49] O. Sologub, L. Salamakha, P. Rogl, B. Stöger, E. Bauer, J. Bernardi, G. Giester, M. Waas, and R. Svagera, Pt-B system re-visited: $\mathrm{Pt_2B}$, a new structure type of binary borides. Ternary $\mathrm{WAl_{12}}$-type derivative borides, Inorg. Chem. **54**, 10958 (2015).

[50] Y. Hinuma, G. Pizzi, Y. Kumagai, F. Oba, and I. Tanaka, Band structure diagram paths based on crystallography, Comput. Mater. Sci. **128**, 140 (2017).

[51] J. A. Blanco, M. de Podesta, J. I. Espeso, J. C. Gómez Sal, C. Lester, K. A. McEwen, N. Patrikios, and J. Rodríguez Fernández, Specific heat of $\mathrm{CeNi_xPt_{1-x}}$ pseudobinary compounds and related dilute alloys, Phys. Rev. B **49**, 15126 (1994).

[52] M. A. Continentino, S. N. de Medeiros, M. T. D. Orlando, M. B. Fontes, and E. M. Baggio-Saitovitch, Anisotropic quantum critical behavior in $\mathrm{CeCoGe}_{3-x}\mathrm{Si}_x$, Phys. Rev. B **64**, 012404 (2001).

[53] S. A. M. Mentink, T. E. Mason, S. Süllow, G. J. Nieuwenhuys, A. A. Menovsky, J. A. Mydosh, and J. A. A. J. Perenboom, Gap formation and magnetic ordering in $\mathrm{URu_2Si_2}$ probed by high-field magnetoresistance, Phys. Rev. B **53**, R6014 (1996).

[54] E. Jobiliong, J. S. Brooks, E. S. Choi, H. Lee, and Z. Fisk, Magnetization and electrical-transport investigation of the dense Kondo system $\mathrm{CeAgSb_2}$, Phys. Rev. B **72**, 104428 (2005).

[55] B. Cornut and B. Coqblin, Influence of the crystalline field on the Kondo effect of alloys and compounds with cerium impurities, Phys. Rev. B **5**, 4541 (1972).

[56] K. Kadowaki and S. B. Woods, Universal relationship of the resistivity and specific heat in heavy-fermion compounds, Solid State Commun. **58**, 507 (1986).

[57] M. E. Fisher and J. S. Langer, Resistive Anomalies at Magnetic Critical Points, Phys. Rev. Lett. **20**, 665 (1968).

[58] H. Yamada and S. Takada, Magnetoresistance of antiferromagnetic metals due to *s*-*d* interaction, J. Phys. Soc. Jpn. **34**, 51 (1973).

[59] P. Schlottmann, Low-temperature magnetoresistivity of Kondo systems: Comparison with experiments on Ce impurities in $\mathrm{LaB_6}$ and $\mathrm{LaAl_2}$, Phys. Rev. B **35**, 5279 (1987).

[60] A. E. Clark, Magnetostrictive rare earth-Fe2 compounds, in *Ferromagnetic Materials*, edited by E. P. Wohlfarth (North-Holland Publishing Company, Amsterdam, 1980), Vol. 1, Chap. 7, pp. 531–589.